Flame-front tracking in Porous Media Burners

Enrique Flores-Montoya, Pierre-Alexandre Masset, Thierry Schuller, Laurent Selle

Flame-front tracking in Porous Media Burners

Enrique Flores-Montoya[a], Pierre-Alexandre Masset[b], Thierry Schuller[a,c], Laurent Selle[a]

[a]*Institut de Mécanique des Fluides de Toulouse, Université de Toulouse, CNRS, Toulouse, 31400, France*
[b]*Université Paris-Saclay, CEA, Service de Thermo-hydraulique et de Mécanique des Fluides, Gif-sur-Yvette, 91191, France*
[c]*Institut Universitaire de France (IUF),*

Abstract

An experimental setup combining computer-generated geometries, additive-manufacturing, a telecentric lens and $CH^\star$ chemiluminiscence is used to visualize the flame inside an optically accessible Porous Media Burner (PMB). As a result, the flame front position inside the burner can be tracked as a function of the operating conditions. Flame tracking is used to analyze the influence of the pore size d_p on the stabilization of lean premixed CH_4-Air flames. $CH^\star$ chemiluminiscence and temperature measurements reveal nearly flat sub-adiabatic flames featuring an axially spread-out reaction region, but with much higher gradients for the heat release rate distribution. In this respect, the localization of the heat release rate provides a significant addition for the validation of Volume Averaged Models (VAMs). A comparison between a state-of-the-art 1D-VAM and the experimental results is proposed in terms of flame position, reaction-zone thickness and temperature profile. A rigorous evaluation of the effective coefficients is performed at the aid of the analytic description of the burner geometry. The model captures fairly well the thermal state of the system as in many previous studies, but exhibits significant deviations for the flame position and its thickness. Scrutinizing the various model parameters, the positioning of the flame inside the burner is found to be extremely sensitive to the interphase heat exchange term. These comparisons call for improvement in combustion models for porous media and suggest that pointwise temperature measurements in multi-stage burners are insufficient for the validation of 1D-VAM if an accurate characterization of the operating domain of the burner is sought.

Keywords: Porous Media Combustion, Additive Manufacturing, Flame Visualization, Optical Access, Volume-Averaged Model

Novelty and significance statement

The novelty of this research is the combination of additive manufacturing techniques with computer-generated geometries to produce an optically accessible Porous Media Burner featuring see-through directions. This burner design, combined with the use of a telecentric lens and $CH^\star$ chemiluminiscence, enables direct flame front visualization.

It is significant because it represents the first non-intrusive tracking of the flame front position as a function of the burner operating conditions. This allows us to compare the flame stabilization in experiments to a 1D-Volume-Averaged Model. Our results bring to light a series of flaws present in state-of-the-art models and question the use of temperature measurements with thermocouples for model validation.

Author Contribution

- E. F. M. Investigation, Software, Data curation, Visualization, Formal analysis, Writing - Original Draft
- P. A. M. Conceptualization, Methodology, Software, Formal analysis, Writing - Review & Editing
- T. S. Conceptualization, Formal analysis, Writing - Review & Editing, Supervision, Funding acquisition
- L. S. Conceptualization, Formal analysis, Writing - Review & Editing, Supervision, Funding acquisition

1. Introduction

Porous Media Combustion (PMC) is a technology based on heat recirculation featuring low pollutants emissions and broad turndown ratios [1, 2, 3, 4]. In Porous Media Burners (PMBs), a flame is stabilized within the voids of an inert solid porous matrix. The upstream recirculation of heat through the solid preheats the fresh reactants enhancing flame stability and broadening flammability limits [5].

The theoretical foundations of excess-enthalpy combustion were established after the seminal works of [6, 7, 8, 9]. Heat recirculating burners are characterized by the multiplicity of solutions, super-adiabatic temperatures and enhanced burning rates. More recently, the theoretical analyses of Pereira et al. [10, 11, 12] and Masset et al. [13, 14] have provided further understanding into the characteristic lengthscales and the different asymptotic regimes, namely, decoupled, hyperdiffusive and intermediate. Theoretical models are key to understand the underlying physical mechanisms at play and provide insight into the stability of solutions, the characteristic lengthscales, the combustion regimes and the governing parameters. From theory, it is known that in homogeneous PMBs there is a relationship between the burning rate and the flame position inside the porous matrix. This distinctive property of heat recirculating burners will be exploited here for model validation. However, theoretical and asymptotic models usually require strong assumptions such as constant transport coefficients and adia-

baticity. As a result, they usually do not provide quantitative results.

On the other side of the spectrum there are Direct-Pore-Level Simulations (DPLS) where the reactive Navier-Stokes equations are numerically solved at the pore scale [15, 16, 17, 18, 19, 20]. This framework resolves all flow features and can in principle account for detailed kinetics, heat diffusion in the solid and radiation. Thanks to currently available computing power and 3D scanning techniques, the computation of actual ceramic-foam burners has been achieved [17, 19, 20, 21].

Despite their accuracy, the large computational cost of DPLS makes them impractical for engineering applications and burner design. More affordable simulations are sought and the so-called Volume Averaged Models (VAMs) offer a relevant alternative between theoretical models and DPLS [22, 23, 17]. In VAMs, equations are averaged over a Representative Elementary Volume (REV) with a characteristic lengthscale of l, which must satisfy two conditions:

$$d_p \ll l \ll L \qquad \text{and} \qquad \Delta_l \psi \ll \Delta_L \psi \tag{1}$$

where d_p is the characteristic pore size, L is the system lengthscale of the system and ψ is a generic variable. These models are generally one-dimensional, yet some remarkable attempts of developing multi-dimensional VAMs can be found in the literature [24]. So far, adiabaticity was a common assumption but the latest models include a sink term in the solid phase equation to incorporate radial heat losses by radiation [25, 26]. Upon the averaging process of the equations, effective properties and transport coefficient arise [27]. These effective coefficients are incorporated to model certain physical phenomena such as dispersion that take place at the pore level scale and whose multi-dimensional and geometry-dependent nature is partially lost in the averaging process. Provided the sensitivity of the model to some of these effective coefficients, part of the modeling efforts are exclusively devoted to come up with accurate and representative submodels for some of these physical phenomena [17, 28, 19, 29, 30, 25]. Model accuracy is not the only concern, as pointed out by many authors [15, 16, 17, 19] DPLS results question the relevance of VAMs assumptions. In these works, it is observed that because of the small thickness, δ_T, of hydrocarbon flames, Eq. (1) does not strictly hold. Regarding experimental validation, the most commonly used diagnostics is pointwise temperature measurements which are generally compared to VAM results in two-staged burner configurations where the flame stabilizes at the interface between two porous layers. It is pointed out that this burner configuration may bias the validation since it essentially imposes the flame-front location. Moreover, in this work, a new technique is presented to complement the temperature measurements.

In experimental studies reticulated ceramic foams are commonly used in PMBs because of the material's high fusion temperature [23, 26, 25, 17]. Unfortunately, their random structure make them opaque, which prevents non-intrusive optical access to the inside of the solid matrix. Nevertheless, there are a few remarkable studies in which optical pathways for laser diagnostics are created. In [31], OH-PLIF was used to visualize the flame front through a narrow slit in a PMB. CARS has also been successfully applied to measure the gas phase temperature in a two-stage combustor [32, 33]. In these works, optical access is very limited and is achieved either by using very large pores or by creating narrow gaps inside the porous matrix and therefore altering the burner geometry. A notable exception is the use of X-ray tomography [23], which allowed the reconstruction of the temperature field in a multi-layer SiC burner. This technique has also been used in combination with infrared thermometry [21] to obtain a full reconstruction of the temperature field in both phases of the burner. Recently, direct visualization of the flame front was achieved in a 2D configuration where optical access was granted by the use of quartz walls and a single-layer packed-bed configuration [34].

The topological parameters of the porous matrix play a major role in flame stabilizaiton [35]. However, when it comes to modeling, random reticulated foams make the characterization of the geometry difficult. If an accurate description of the matrix is sought, X-ray tomography is required to scan a small sample of the porous structure [26, 19, 17, 21, 25]. This technique is expensive and not exempt of technical difficulties. Concerning the burner design, off-the-shelf ceramic foams are usually arranged in a staged configuration, with two or more layers of different pore size. Nevertheless, some recent studies have shown that a graded topology could be used to optimize the burner performance [36, 37]. An alternative to reticulated foams is the combination of computer-generated geometries with Additive Manufacturing (AM) techniques. This option enables topology tailoring and has already been successfully applied to enhance the burner operating range via spatial topological gradation in lattice-based porous structures [38, 35].

In this work, a new experimental technique and a validation method for PMBs is proposed. This validation technique consists in the tracking of the reaction zone inside the burner as function of the operating conditions. It relies on a basic principle of heat recirculating burners: the relationship between the flame position and the burning rate in a homogeneous porous media. To accomplish the tracking of the reaction region, optically accessible burners are conceived and tested. These are made possible by the combination of computer-defined topologies and Additive Manufacturing techniques. The topologies used here feature see-through directions that enable direct flame-front visualization and hence the tracking of its position. The novel experimental setup presented here uses a telecentric lens to measure the axial distribution of $CH^\star$ chemiluminiscence. Topology tailoring offers a systematic control of the geometrical parameters of the porous matrix, which is here exploited to assess the influence of the pore-size on flame stabilization.

The results are compared with a 1D VAM where the effective properties and model parameters are evaluated from the mathematical definition of the geometry. Despite the detailed description of the models made in this work, the purpose is not to make a contribution to VAM modeling. The models presented are state-of-the-art and the reason for such a careful evaluation of the various parameters is to show that this is not the cause for the deviation from the experimental results. A direct com-

parison in terms of flame front position, reaction region thickness and temperature profiles is performed. The results point out several shortcomings in the state-of-the-art VAMs and may call for a revision of the diagnostics currently used for validation. The remainder of the article is organized as follows: Section 2 describes the experimental setup and procedure; Section 3 presents the 1D-VAM and details the evaluation of the model parameters. The comparison between the experimental and numerical results is offered in Section 4. Finally, Section 5 summarizes the main findings and discusses paths for improvement.

2. Experimental setup & procedure

As a preliminary remark, many studies comparing experimental results and 1D VAM numerical solutions are performed with two-layer PMBs with different pore sizes. The stage with smaller pores is placed upstream so that the flame cannot flashback and is often stabilized at the junction between the two layers. This reduces the coupling between the flame front position and the heat recirculation so that it is arguably a less stringent validation than the PMBs with homogeneous properties used in the present work.

2.1. The POROSITO test rig.

Figure 1 presents the POROSITO test rig: at the bottom, methane and air flows are imposed via two Bronkhorst ELFLOW mass flow controllers. The premixed reactants go through a convergent section and a sintered steel plate to remove flow inhomogeneities. To limit the thermal drift of the system, the straight duct section is cooled down to $T_w = 293$ K. Nevertheless, the radiative heat flux from the burner heats up the sintered steel plate and the fresh gases. A K-type thermocouple is used to measure the actual temperature of the reactants, T_{in}, which serves as the reference for the laminar flame properties at each operating point. Then, the PMB leans on an inner quartz tube and is enclosed by another quartz tube with inner diameter $D = 50$ mm. To minimize the leakage between the quartz and the burner, the quartz-to-porous gap is smaller than the pore size at room temperature conditions. Graphite joints between the different components are used for sealing and the ensemble is clamped by an upper flange.

2.2. Optically accessible burners

Selective Laser Melting (SLM) [39] is employed to produce a cylindrical porous matrix made of 316L stainless steel alloy. This metal features a high resistance to corrosion at elevated temperatures and its solidus temperature is 1648 K. The burner geometry is generated via an in-house Python code. Its fluid-solid interface is defined by a Diamond Triply-Periodic Minimal Surface (TPMS) [40, 41, 42], following the implicit equation:

$$s(\kappa x)s(\kappa y)s(\kappa z) + s(\kappa x)c(\kappa y)c(\kappa z) + c(\kappa x)s(\kappa y)c(\kappa z) + c(\kappa x)c(\kappa y)s(\kappa z) = t \quad (2)$$

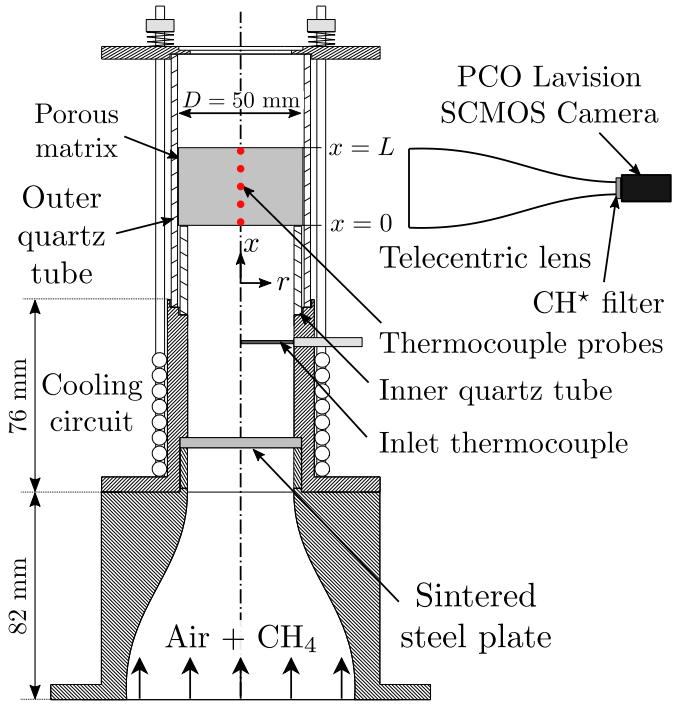

Figure 1: Schematic of the POROSITO test rig.

where $s(\cdot)$ and $c(\cdot)$ stand for the sin(·) and cos(·) functions, respectively. Void fraction, ϵ, and pore size, d_p, are controlled by the threshold, t, and the wavenumber, $\kappa = 2\pi/\Lambda$, in Eq. (2). In the present study, three PMBs with porosity $\epsilon = 0.8$ and different pore sizes are considered. The height of the burner is $L = 30$ mm. The x axis is oriented in the streamwise direction and its origin is at the burner inlet. The streamwise coordinate is often expressed in dimensionless form by normalizing with the burner length, $\xi = x/L$. The resulting geometry features several see-through directions in 3D, allowing multiple optical accesses inside the porous matrix.

Many experimental studies using topology-tailoring [35, 38] are focused on the operational advantages of this manufacturing technique such as the optimization of burner performance via topological gradation. However, a peculiarity of TPMS-based topologies is the existence of See-Through Directions (STD) in the porous matrix. These matrices feature multiple parallel optical pathways here called See-Through Directions. These optical pathways provide extensive access for optical diagnostics. As a result, direct visualization of the flame inside the burner is possible. Optically accessible burners represent the major novelty of the present work. Depending on which TPMS is used the optical pathways of the burner are arranged differently. Some of these optical pathways, here called minor, are too small for practical purposes. Moreover, porosity can affect the number of usable STDs. In the Diamond topology, there are four major and three minor (STDs). Figure 2a sketches the arrangement of the STDs in the Diamond topology. Two of the major STDs are contained in the XZ and the XY planes and are not shown in Fig. 2a since they are not used in the present work. The other two major STDs – here referred to as yz and zy – are horizontal

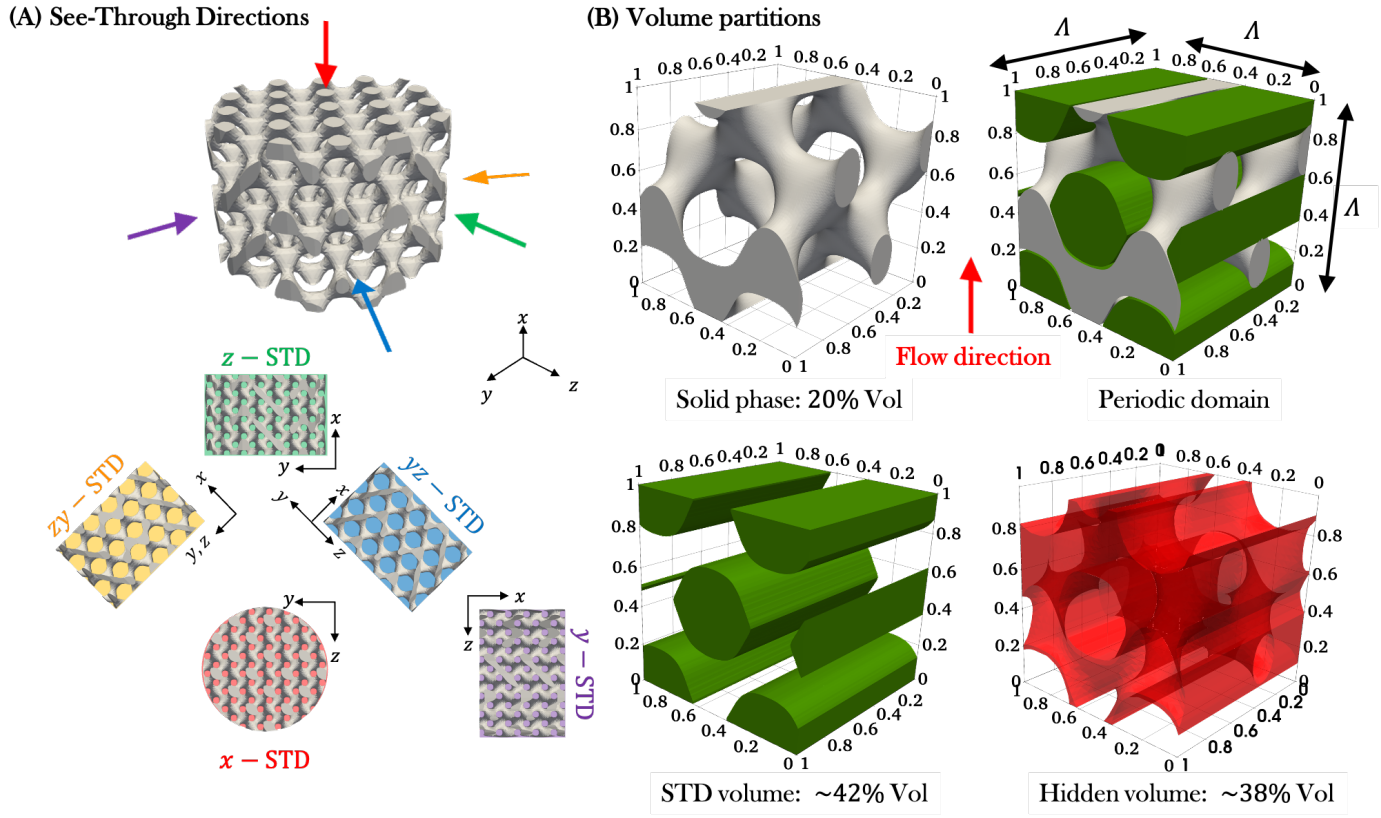

Figure 2: A) Arrangement of the STDs in a Diamond-TPMS-based porous media. In this topology, the x, y and z-STD are too small for practical purposes. For direct flame visualization, the zy and the yz-STD can be used to access the interior of the porous matrix. B) 3D view of the different volume-partitions in an elementary volume. Green-colored volumes are accessible by imaging the porous media from one of the major STDs and represent roughly 42% of the total volume. The hidden volume is depicted in red an accounts for approximately 38% of the total volume. The remaining 20% of the volume is occupied by the solid phase.

and are employed here for direct flame visualization.

A detailed view of the STD is offered in the 3D rendering on Fig. 2b. The represented volume extends for one wavelength in the three directions of space. With this topology, if only one major STD is used, the optically accessible volume represents approximately 42% of the total volume, which is more than half of the gas-phase volume. Finally, the hidden volume, which is the fraction of the gas phase that cannot be seen is roughly 38% of the total volume. In contrast to previous efforts [31, 32, 33], the present technique offers an extensive optical access to the interior of the porous matrix.

2.3. Diagnostics

The STDs are also used to insert thermocouples that are placed along the symmetry axis of the burner at different longitudinal positions. N-type thermocouples with a sheath diameter of $d_s = 0.5$ mm are employed. Thermocouples spacing is imposed by the porous matrix periodicity. Given that there are two optical pathways per wavelength, the uncertainty in their positioning is given by $\pm\Lambda/2$. Inside the burner, thermocouple probes are submitted to a significant radiative flux from the solid matrix. The temperature of the thermocouple is given by the convective-radiative equilibrium of the thermocouple's bead at a given location. As a result, temperature readings lie somewhere between the solid and the gas phase temperatures whenever a thermal unbalance between the phases exists.

A LaVision Imager sCMOS camera is used to visualize the flame inside the porous matrix. Images resolution is 2560×2100 px, pixel size is 6.5 μm and images bit-depth is 16 bits. The camera is fitted with an Edmund optics band-pass filter with a bandwith of 10 nm and a central wavelength of $\lambda = 430$ nm to collect the line-of-sight integrated $CH^\star$ radical emission. This allows us to identify the reaction region and to partly remove the black body radiation from the solid, which takes place primarily in the IR and low-frequency visible range.

The imaging system is aligned with one of horizontal the see-through directions of the burner (yz-STD or zy-STD). Due to perspective distortion, if a conventional lens is used, only the optical pathway aligned with the camera direction is completely cleared. To circumvent this issue, the camera is fitted with an Opto Engineering Telecentric lens TC4M-64. This lens features a working distance of 182 mm and a field of view of approximately 60 × 44 mm given the dimensions of the camera sensor. Telecentric (TC) lenses remove perspective distortion providing an orthogonal projection of the imaged objects. Thanks to TC lens, we obtain a cleared optical access for all the visual pathways aligned with the observation STD so there is no need to translate the camera when the position of the flame changes. Figure 3 compares the visualization of the flame using

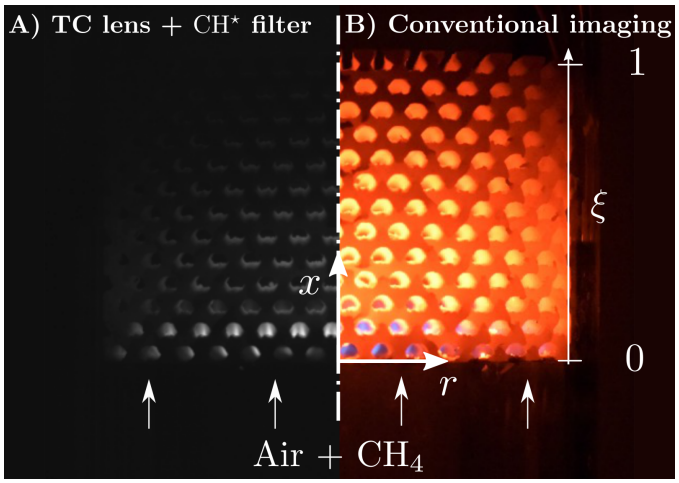

Figure 3: Comparison between a conventional imaging and CH* chemiluminiscence with perspective removal used in the present work.

the present setup and a conventional imaging system. Unfortunately, despite the use of a TC lens, the curvature of the quartz tube causes some distortion of the image at the burner edge owing to light refraction. This reduces the effective visualization through the optical pathways on the sides of the porous matrix.

2.4. Experimental procedure

The operating conditions are defined by the equivalence ratio, ϕ, and the thermal power, P. The maximal absolute uncertainty in the equivalence ratio is $\delta\phi = \pm 0.02$ and the relative error in P is always smaller than 3%. The burner is operated at fixed power, and its operating domain is explored by varying the equivalence ratio in steps of $\Delta\phi = 0.02$. Close to the blowoff and flashback limits, the step is reduced to $\Delta\phi = 0.01$. The flashback limit was rarely reached since the burner maximal operating temperature was usually attained before. When the operating point of the burner is changed, temperature monitoring is used to ensure that a steady state is reached. The burner characteristic settling time is governed by thermal diffusion in the solid phase. Therefore, convergence times typically range between 5 and 15 minutes but can rise to nearly 30 minutes in the vicinity of blowoff. Thermal balance is assumed when the temperature variation registered over two minutes is smaller than 1 K for all the thermocouple probes. For each operating point, once thermal equilibrium is reached, the mass flow controllers and thermocouples signals are recorded and averaged for over two minutes and an image of the flame inside of the burner is taken with an exposure time of 2 s. Finally, a back-lighting placed behind the burner is employed to generate a mask that is used in the post processing stage to remove reflections of CH* signal on the burner surface.

Images are processed to derive the transversely averaged distribution CH$^\star(x)$, which is fitted by a beta-prime function for subgrid interpolation. The details of this post-processing can be found in Appendix A The flame position, x_f, is given by the location of the CH$^\star(x)$ maximum. For each operating point, (ϕ, T_{in}), the laminar burning velocity, S_{L_0}, flame thermal thickness, $\delta_{T_0} = (T_{ad} - T_{in})/\max(\partial T/\partial x)$, unburned gas density, ρ_{in}, and adiabatic flame temperature, T_{ad}, of the corresponding premixed one-dimensional unstretched flame are computed using Cantera. Temperatures are normalized as, $\theta = (T - T_{in})/(T_{ad} - T_{in})$.

3. Numerical methods

The methodology for the computation of flames in PMB is now described as thoroughly as possible since small details actually matter a lot. In the spirit of [25] a systematic literature review was conducted to incorporate the most widely-used submodels for dispersion, interphase heat transfer and radiation. Also, the numerical parameters are chosen with care and those that are geometry-dependent have been evaluated from the 3D representation of the analytic geometry. It is one of the objectives of this work to test standard VAM models in the canonical case of a homogeneous burner. This comparison is arguably more arduous than the widely used two-layer PMBs where the location of the flame is almost fixed by the topological change at the interface between the two porous matrices.

The open source code Cantera [43] has been modified to be coupled with the VAM equations for the solid phase. The detailed kinetic scheme GriMech 3.0 [44] with mixture-averaged transport coefficients is used to model the chemistry of methane-air flames. The computational domain extends from the burner inlet at $x = 0$ to its outlet at $x = L$.

3.1. Equations and boundary conditions

The 1D volume-averaged equations for species and energy conservation in the gaseous and solid phases read [45, 28, 17]:

$$\epsilon\rho u_g \partial_x Y_k + \partial_x\left(\epsilon J_k^{\text{eff}}\right) - \epsilon\dot{\omega}_k = 0 \tag{3}$$

$$\epsilon\rho_g c_{p_g} u_g \partial_x T_g + \epsilon\left[\sum_k c_{p_g,k} J_k^{\text{eff}}\right]\partial_x T_g \tag{4}$$

$$-\partial_x\left[\epsilon\lambda_g^{\text{eff}}\partial_x T_g\right] - h_V\left(T_s - T_g\right) - \epsilon\dot{\omega}_T = 0$$

$$-\partial_x\left(\lambda_s^{\text{eff}}\partial_x T_s\right) - h_V\left(T_g - T_s\right) + \dot{q}_{\text{loss}} = 0 \tag{5}$$

where Y_k are the species mass fractions and T_g and T_s the gas and solid temperatures, respectively. In Eqs. (3)-(5), ϵ denotes the local porosity, ρ the gas density, c_{p_g} the mixture-averaged specific heat, $c_{p_g,k}$ the $k^{th}-$species heat capacity and u_g the gas velocity. The terms $\dot{\omega}_T$ and $\dot{\omega}_k$ denote the heat release rate and the mass production rate of species k per unit volume, respectively.

Dispersion is modeled via effective diffusion coefficients for species and heat transport:

$$J_k^{\text{eff}} = -[\rho W_k(D_k/\tau_g + D^{\text{dis}})\partial_x X_k]/W \tag{6}$$

$$\lambda_g^{\text{eff}} = \lambda_g/\tau_g + \rho c_{p_g} D^{\text{dis}} \tag{7}$$

where W_k and X_k stand for the species molar mass and molar fraction, D_k is the mixture-averaged diffusion coefficient and W is the mean molar mass of the mixture. In Eq. (7), λ_g is the thermal conductivity of the gas, τ_g is the gas phase tortuosity and $D^{\text{dis}} = u_g d_p/2$, is the dispersion diffusion coefficient. Entrance effects upon dispersion coefficient are modeled via a

relaxation distance of two pore sizes where dispersion diffusivity increases from zero to its nominal value [46]. The interphase heat exchange between the gas and the solid is modeled via a volumetric interphase heat coefficient,

$$h_V = \lambda_g S_v \mathrm{Nu}/d_p \tag{8}$$

Here, S_v denotes the interphase surface per unit volume and Nu is a Nusselt number. Many empirical and theoretical correlations have been proposed to model Nu in this framework [47, 29, 30, 48, 17]. Here, the correlation derived in [29] for laminar flows over an array of squared rods is employed, which reads:

$$\begin{aligned} \mathrm{Nu} = (1-\epsilon)^{-1/2}\{1 + 4(1-\epsilon)/\epsilon \\ +(1-\epsilon)^{1/2}\,[(1-\epsilon)^{1/2}\,Re]^{0.6} Pr^{1/3}/2\} \end{aligned} \tag{9}$$

where $Re = u_g d_p/\nu$ and $Pr = \mu c_{p_g}/\lambda_g$ are the pore-based Reynolds and Prandtl numbers, respectively. Because of the strong sensitivity of the flame position to this submodel, the influence of the interphase heat transfer correlation is addressed in Sec. 4. The effective thermal conductivity in the solid includes a tortuosity coefficient and a radiation term:

$$\lambda_s^{\mathrm{eff}} = (1-\epsilon)\lambda_s/\tau_s + \lambda_s^{\mathrm{rad}} \tag{10}$$

If the porous medium is assumed to be optically thick, solid-to-solid radiation can be modeled using the Rosseland approximation [36, 28, 17]:

$$\lambda_s^{\mathrm{rad}} = 16\,\sigma_B\,T_s^3/3\beta \tag{11}$$

where σ_B is the Stephan-Boltzman constant and $\beta = 3/d_p(1-\epsilon)$ is the effective radiative extinction coefficient. Finally, a heat loss term is included in the solid phase energy equation to account for radiative losses through the burner walls:

$$\dot{q}_{\mathrm{loss}} = 4\eta\Xi\sigma_B(T_s^4 - T_{\mathrm{amb}}^4)/D \tag{12}$$

Here, Ξ if the solid phase emissivity, η is the quartz transmissivity and T_{amb} is the ambient temperature.

At the burner inlet, mass flow rate, $\dot{m}_{in}$, mixture composition, $Y_{k_{in}}$, and temperature, T_{in}, are imposed as follows:

$$\dot{m}_{in} - \epsilon\rho u_g\big|_{x=0^+} = 0 \tag{13}$$

$$\dot{m}_{in}Y_{k_{in}} - \epsilon\rho u_g Y_k\big|_{x=0^+} - \epsilon J_k^{\mathrm{eff}}\big|_{x=0^+} = 0 \tag{14}$$

$$\dot{m}_{in}T_{in} - \epsilon\rho u_g T_g\big|_{x=0^+} + \epsilon\frac{\lambda_g^{\mathrm{eff}}}{c_{p_g}}\partial_x T_g\big|_{x=0+} = 0 \tag{15}$$

Equations (13) - (15) assume a balance between convective and diffusive terms upstream of the burner inlet. At the outlet, $x = L$, zero temperature and species gradients are imposed. In the solid phase, radiative heat losses are prescribed on the sides of the domain, $x = x_b$:

$$\Xi\,\sigma_B\left[T_s^4|_{x=x_b} - T_\infty^4\right] = \pm\lambda_s^{\mathrm{eff}}\partial_x T_s\Big|_{x=x_b} \tag{16}$$

where $x_b = 0$ or $x_b = L$ and the sign is given by the direction of the boundary (inlet +, outlet −).

3.2. Evaluation of effective properties

The VAM presented above must be fed with several numerical values that depend on the topology and material of the porous matrix. Topological parameters include the void fraction, ϵ, the pore size, d_p, the specific surface, S_v, and the solid/gas phase tortuosities, τ_s and τ_g, respectively (Tab. 1). Since the geometry is defined by a mathematical function, these properties can be evaluated a priori with good accuracy. Pore size, d_p, and fluid and solid tortuosities, τ_g and τ_s are computed from a voxel representation of the geometry using the python tool Porespy [49]. For a given point, $\mathbf{x}$ in the gas phase, the local pore size is defined as the diameter of the largest sphere that contains $\mathbf{x}$ and is tangent to the solid phase. Note that the sphere is not necessarily centered on $\mathbf{x}$. The global pore size, d_p, is obtained as the pore diameter for which the pore size distribution is maximum. Tortuosity is computed as the ratio between the effective and the intrinsic diffusivity weighted by the phase porosity in purely Fickian diffusion simulations [49, 50]. The volumetric surface of the porous matrix is computed from a triangulated representation of the geometry.

Material-dependent parameters include the solid thermal conductivity, λ_s, the solid emissivity Ξ and the quartz transmissivity, η. Selective Laser Melting (SLM) has been used to 3D-print the porous burners for this study. Owing to the manufacturing process, the thermo-mechanical properties of the resulting solid component slightly differ from those of the bulk base material [51]. Metallic samples feature a certain level of intrinsic porosity which results in a mildly lower themal conductivity. Use made of the printing parameters (hatching, laser scanning speed...) we have estimated a value of the energy density of approximately 36 J mm^{-3}. Following [51], we can expect a level of intrinsic porosity between $0-5$ % and a drop in the through-plane thermal conductivity of the material from roughly 15 W m^{-1} K^{-1} to approximately $\lambda_s = 13$ W m^{-1} K^{-1} at room temperature conditions.

For the solid emissivity Ξ, a number of experimental and numerical works have studied the emissive properties of 316L samples under different pressures, temperatures, surface state and oxidation conditions [52]. There is a vast disparity in the emissivity values depending on the surface roughness and the level of oxidation of the samples. Due to the manufacturing process and the extreme operating conditions of the burner, their surface is oxidized and rough. Given the typical temperatures measured inside the burner ($1000-1300$ K), we can estimate the emissivity to fall within $0.6 < \xi < 0.7$. Henceforth, a value of $\xi = 0.65$ is retained for the emissivity of the solid phase. Quartz transmissivity, η_λ, depends upon the light wavelength, λ_r. Typically, quartzs are fully transparent ($\eta_{\lambda_r} = 1$) within the wavelength range 150 nm $< \lambda_r <$ 3000 nm and opaque elsewhere ($\eta_{\lambda_r} = 0$). The total transmissivity, $\eta(T)$, is thus a function of the temperature of the solid and can be computed as,

$$\eta(T) = \left(\int \pi\eta_{\lambda_r} B(\lambda_r,\,T)\mathrm{d}\lambda_r\right)/\left(\sigma_B T^4\right) \tag{17}$$

For solid temperatures between 800 K $< T_s <$ 1400 K the transmissivity varies almost linearly between $0.14 < \tau < 0.52$.

d_p [mm]	ϵ	S_v [m^{-1}]	τ_g	τ_s
1.5		1215		
2.5	0.8	729	1.19	2.52
3.5		521		

Table 1: Topology-dependent parameters

4. Results & Discussion

Figure 4 plots the experimental points evaluated in this study in the $P - \phi$ map. The blowoff, flashback and high temperature limits are indicated with dotted, solid and dashed lines, respectively. The shadowed region delimits the estimated boundaries of the burner operating domain. Dashed areas on the upper right corners indicate unexplored regions due to thermal constrains. The blowoff limit is unaltered when the pore size is reduced from $d_p = 3.5$ mm to 2.5 mm but is shifted towards higher equivalence ratios when d_p is decreased to 1.5 mm. This greatly impacts the burner operating range at the lower pore size.

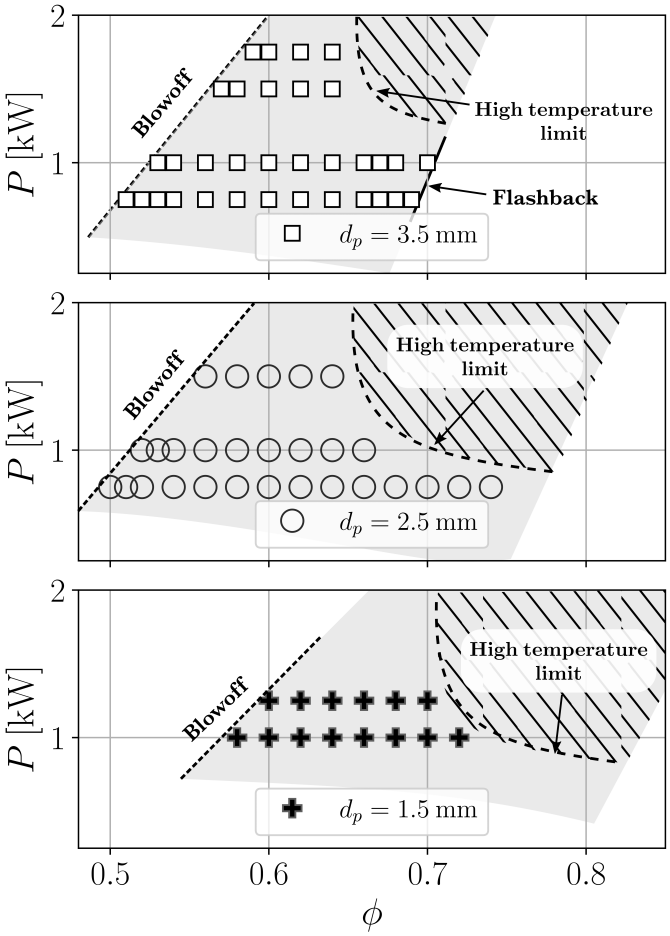

Figure 4: Operating domain of the PMBs for different pore sizes, d_p, spanned by power, P, and equivalence ratio, ϕ.

Figure 5 illustrates how the new method presented here allows the determination of the flame front position. Three flames at the blowoff limit with $P = 1$ kW stabilized in PMBs with different pore sizes are shown. On the left, direct visualizations where the white dotted lines indicate the interpolated flame position. At the center, the profiles of CH* in red dotted lines and the beta-prime fit of the experimental curve in black dashed lines. The solid blue line is the normalized heat release rate profile computed with the VAM solver for the same operating conditions. Finally, in the right column, the experimental and numerical normalized temperature profiles. At the blowoff limit, flames are observed approximately in the middle of the porous matrix. For the $d_p = 3.5$ mm and $d_p = 2.5$ mm PMBs, the flame spreads over two and three pore rows respectively. However, the width of the reaction region remains approximately constant. When the pore size is reduced to $d_p = 1.5$ mm the width of the flame front increases and the reaction zone is distributed over 5 to 6 pore rows. Regardless of the pore size and the burner load, there is limited radial deformation of the reaction region so that the comparison with 1D simulations seems quite reasonable.

There are large discrepancies between the heat release rate profiles computed using the VAM and the experimental CH* distribution. Both the width and the position of the peak are not well predicted by the model. In experiments, the width of the reaction region is several times larger than in simulations. Direct pore-level simulations [19] have shown wrinkled flames distributed over several pores as a result of local anchoring effects. Owing to the line-of-sight integration of the CH* signal, such a flame front would appear to be thickened with the present experimental setup. Therefore, we cannot infer whether the thickening results from a local broadening of the reaction region or from the spatial averaging of a thin wrinkled flame front. Nevertheless, it appears that additional modeling efforts are needed in VAMs to predict the extent and position of the reaction region. It is reiterated that unlike in two-layer PMBs with different pore sizes, here the flame is not preferentially anchored at the interface. This allows for a two-way coupling between combustion and heat recirculation, which arguably makes it a more stringent validation case for VAMs. Regarding the temperature profiles, there is a fair agreement between the measurements and the model. The offset in the flame position between the model and the experiments yields significant errors upstream of the flame but the maximum temperatures and the temperature gradients at the outlet show a reasonable agreement. This indicates that, overall, thermal losses are well modeled in the simulations. Interestingly, despite the blatant disagreement in the heat-release rate profiles, the fair agreement observed in the temperature profiles suggests that this variable is actually less sensitive to changes in the inlet mass flow rate.

The evolution of the flame position with the operating conditions is now analyzed. For each experiment, the streamwise momentum is computed as, $\dot{m} = \rho_{in} u_B = \dot{M}/A\epsilon$, where $A = \pi D^2/4$, $\dot{M}$ is the total mass flow and u_B is the bulk velocity in the burner. This value is normalized by the mass consumption rate per unit surface of a planar unstretched flame defined as, $\dot{m}_0 = \rho_{in} S_{L_0}$. The ratio, $\dot{m}/\dot{m}_0$, quantifies the increase in mass consumption rate per flame unit surface and is called here the *flame speed-up*. As for the experiments, the position of the

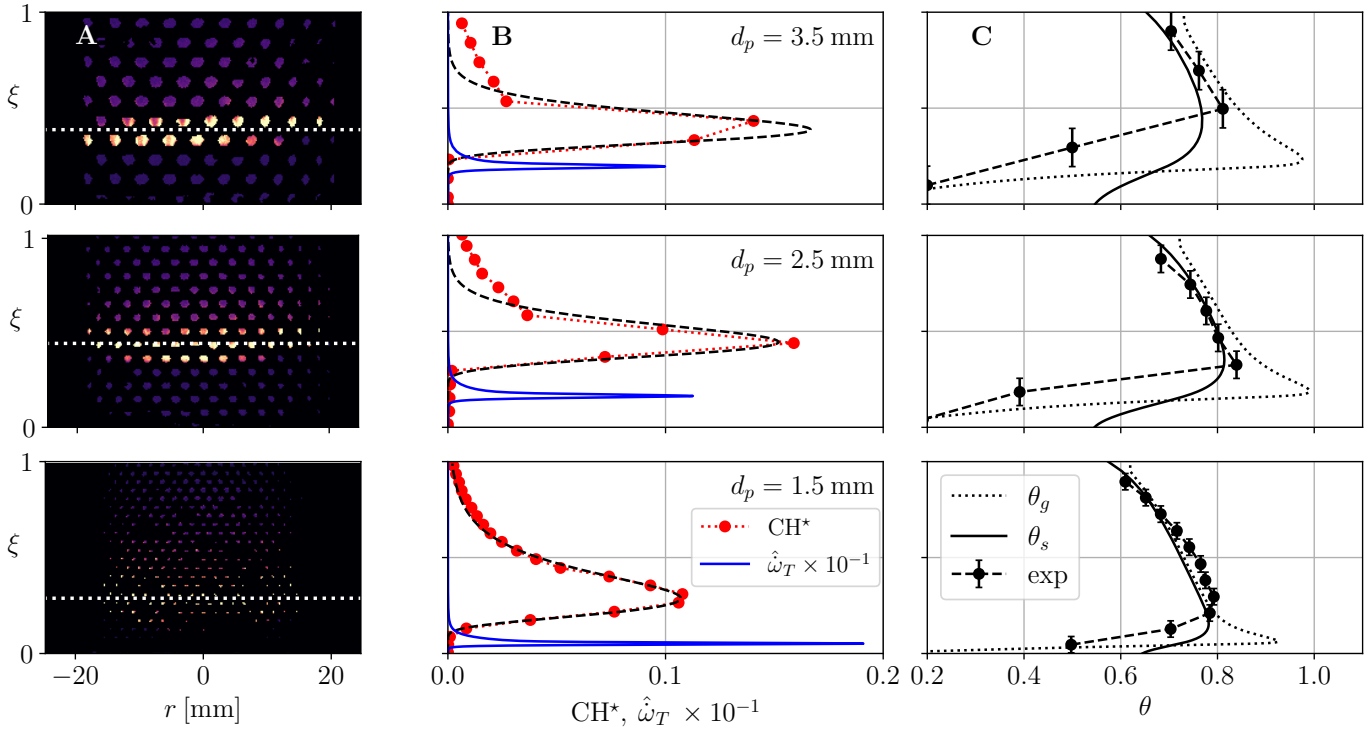

Figure 5: Flame structure for cases at the blowoff limit with $P = 1$ kW. A) Image of CH⋆. B) Profiles of CH⋆ from the experiment and normalized heat release rate $\hat{\omega}_T$ from simulations. C) Experimental and computed normalized temperature profiles. Results in (B) and (C) are presented as a function of $\xi = x/L$.

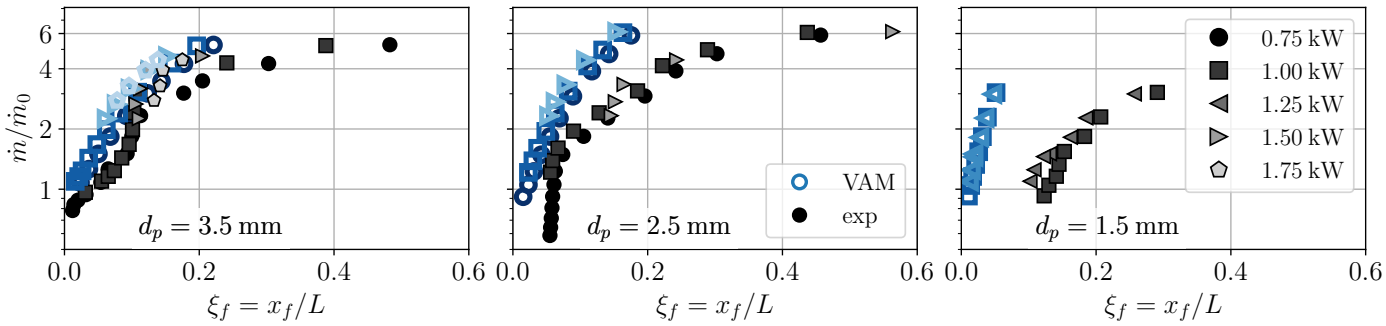

Figure 6: Flame speed-up, $\dot{m}/\dot{m}_0$, versus flame position, $\xi_f = x_f/L$, for different powers and pore sizes, d_p. The h_V correlation presented in Kuwahara et al. [29] is used as interface heat exchange submodel.

flame in the burner, x_f, is defined by the location of the heat release rate maximum. In the simulations, when the flame is so close to the inlet that the heat-release-rate is non-zero on the boundary condition, the case is considered to be a flashback. In practice, flashback is influenced by entrance, boundary layer effects and local pore-anchoring. Therefore, its quantitative prediction is more complex and out of the scope of the present work. Here, the focus is on the overall agreement between the observed and computed flame position for a given mass flow rate.

Figure 6 shows the speed-up, $\dot{m}/\dot{m}_0$, versus the dimensionless flame position, $\xi_f = x_f/L$, at different powers for the three burners. When the flames are close to the inlet, $\dot{m}/\dot{m}_0 \simeq 1$, which is consistent with the limited preheating. Because of thermal losses, the speed-up can even be smaller than unity near $\xi = 0$. As the bulk to flame velocity ratio is increased, the position of the flame is shifted towards the burner outlet. The speed-up reaches a maximum value at approximately $\xi \simeq 0.5$. At this point, a further increase of u_B/S_{L_0} leads to blowoff. This is, to the authors' best knowledge the first tracking of the flame front position as a function of the burner operating conditions. These experimental observations confirm the theoretical predictions obtained with analytical models for finite porous media [8, 13]. The flame position is found to be independent of the thermal power for the range reported in this study. Interestingly, despite sub-adiabatic temperatures are measured inside the burner, the mass consumption rate per unit surface of the flame increases by nearly a factor six at blowoff in the $d_p = 2.5$ mm burner. This ratio is reduced to approximately three in the $d_p = 1.5$ mm case. For the experimental results at hand, the speed-up at blowoff is found to decrease when the pore size is reduced. Concerning the flame positioning, a fairly good agreement between the

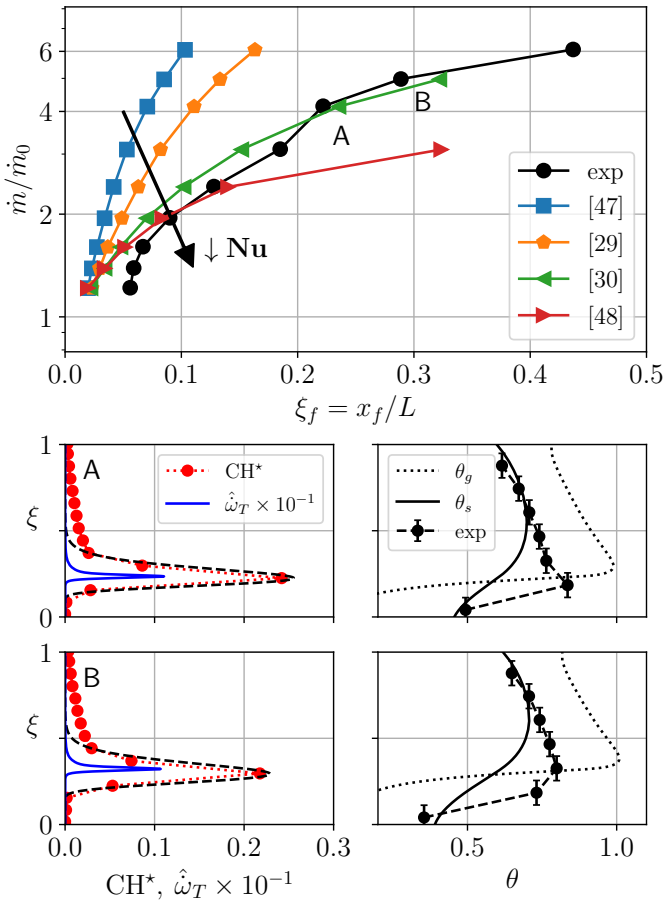

Figure 7: Influence of the interphase heat exchange term.

model and the experiments is obtained for $d_p = 3.5$ mm. However, near blowoff differences between the model and the experimental results significantly increase. As the pore size is decreased, the agreement between the experimental results and the model progressively degrades. At $d_p = 1.5$ mm, the predicted flame position is completely off the experimental observations. Interestingly, in simulations, the influence of the thermal power on the position of the flame is also marginal and qualitatively similar to experiments. In experiments, the pore size plays a major role in flame stabilization influencing both the position and the width of the reaction zone. This strong influence does not seem to be captured by the model where the stabilization curves are marginally affected by changes in d_p.

In an effort to identify paths for improvements of the simulations, the sensitivity to the interphase heat transfer model is now discussed. To this end, the position of the flame is computed using several correlations from the literature [29, 30, 47, 48]. Results are plotted in Fig. 7 for a 1 kW flame in the $d_p = 2.5$ mm burner. As the Nusselt number decreases, flames stabilize further downstream for a given flow rate. Using the correlation proposed in [30], the current 1D model accurately predicts the flame position. The use of this correlation improves the numerical predictions for $d_p = 2.5$ mm and $d_p = 3.5$ mm. However, it does not perform as well for the $d_p = 1.5$ mm burner (see Fig. 8). Figure 7 compares the experimental and simulated streamwise profiles for two mass flow rates. The heat release rate profiles show an excellent agreement in terms of mean flame position. However, the model still fails to predict the thickness of the reaction region. Furthermore, the numerical results show large differences between the solid and the gas phase temperatures suggesting the operation in the so-called decoupled regime [53]. It is pointed out that the correlation from [30] was derived and validated for turbulent flows with $10^4 < Re < 10^7$ while in the present experiments, the pore-based Reynolds number falls within $20 \lesssim Re \lesssim 120$. This strongly questions the use of the correlation and might indicate some kind of error compensation between the submodels. This question should be addressed in future works since it has a major impact on the blowoff limit of the burner. Further efforts must also focus on the thickening of the reaction region and the influence of the pore size, which are not well retrieved by the 1D model.

5. Conclusion

In this work, direct visualization of the flame front inside a porous medium has been achieved by means of a brand-new experimental setup that combines computer-defined topologies, AM techniques, TC optics and CH* chemiluminiscence. For the first time, the position of the reaction region inside a PMB could be directly tracked as a function of the operating conditions enabling a better confrontation between experiments and simulations. The combustion of lean methane-air flames has been analyzed for three PMBs with different pore sizes. The experimental results show nearly one-dimensional sub-adiabatic flames featuring a thickened reaction region.

Comparisons are carried out with a state-of-the-art VAM with detailed chemistry and including radial heat losses. Effective parameters are evaluated by making use of the exact description the burner geometry and correlations from the literature. Neither the width nor the position of the reaction zone are accurately predicted by the VAM, specially for small pore sizes. In contrast, heat losses are well estimated and a reasonably good agreement is obtained for the temperature profiles. Finally, the effect of the interphase heat exchange term on the positioning of the flame has been shown to have a strong impact on the flame position. In previous studies, VAM are typically validated using pointwise temperature measurements in multi-stage burners where the flame usually stabilizes at the interface between two layers. The results presented here show that a qualitative agreement between the temperature profiles can be achieved if global heat losses are well characterized. In contrast, predicting the flame position inside the burner, which is necessary for accurate description of the blowoff limit, is much more challenging. The present work highlights that current VAMs exhibit high sensitivity to the modeling of the heat exchange term, failing to accurately predict both the flame thickness and the impact of the pore size.

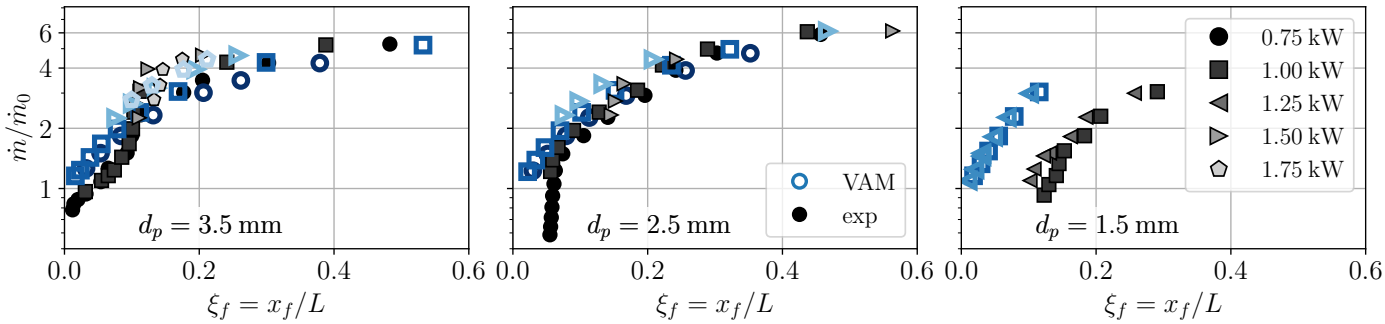

Figure 8: Flame speed-up, $\dot{m}/\dot{m}_0$, versus flame position, $\xi_f = x_f/L$, for different powers and pore sizes, d_p. The h_V correlation presented in Saito and De Lemos [30] is used as interface heat exchange submodel.

Acknowledgments

The PhD of Enrique Flores Montoya is funded by BULANE and the Occitanie Region (*Défi Clé Hydrogène Vert*). Vincent Baylac (CIRIMAT) and Sebastian Cazin (IMFT) are acknowledged for their technical support with the manufacturing of the PMBs and the optical diagnostics, respectively. This project has received funding from the European Research Council (ERC) under the European Union's Horizon 2020 research and innovation programme, Grant agreement No. 832248, SCIROCCO.

Appendix A. Images post-treatment

This sections describes the procedure to extract the axial CH* profile from chemiluminiscence images. Overall, the post-treatment method is very robust and requires only minor adjustments when the pore size is changed.

When projected onto the camera sensor, the optical pathways of the burner generate a two-dimensional array of spots. This is illustrated in Fig. A.9 where a backlight image is shown. Here, the reduction in visualization surface on the sides caused by light refraction is made evident. The CH* emission by the flame is integrated along the optical pathways and collected by the sensor. Figure A.9b shows a CH* chemiluminiscence image where the row of bright spots indicates the overall position of the flame. The backlight image is binarized and used to mask the CH* chemiluminiscence signal. This allows us to rule direct reflections out. The masked image is transformed into a matrix representation where each element stores the surface-weighted average of the CH* intensity on each spot of the 2D pattern A.10. By weighting the average by the surface we can remove the influence of occasional artifacts in the images and the radial deformation by refraction. This matrix form is then used to compute the radial and axial profiles of CH* so that the resolution of these raw profiles is given by the spacing between the pores. Since, the CH* often spans over more than one row of optical pathways, to smooth the flame front tracking we fit the raw axial profiles by a betaprime distribution. The position of the flame front, x_f, is given by the location of the CH$^\star(x)$ maximum.

Concerning the radial profiles, we observe a reduction of the intensity of the CH* signal towards the edges of the burner. This lack of radial homogeneity can be explained by the Line-of-Sigth (LoS) integration of the CH* emission. The integration path is maximal for the central optical pathways and reduces as we move towards the burner sides. The raw radial profile can be corrected by normalizing the radial distribution by the length of the integration path at each r. Despite this correction is somewhat rudimentary because it assumes a transverse homogeneity of the signal, the corrected radial profiles are rather homogeneous indicating that the assumption holds. The radial homogeneity of the CH* profiles suggest that the comparison with a 1D model is reasonable.

References

[1] S. Wood, A. T. Harris, Porous burners for lean-burn applications, Prog. Energy Combust. Sci. 34 (2008) 667–684.

[2] M. A. Mujeebu, M. Z. Abdullah, M. Z. Bakar, A. A. Mohamad, M. K. Abdullah, Applications of porous media combustion technology - A review, Appl. Energy 86 (2009) 1365–1375.

[3] M. Weclas, Potential of Porous-Media Combustion Technology as Applied to Internal Combustion Engines, J. Thermodyn. 2010 (2010) 1–39.

[4] J. Ellzey, E. Belmont, C. Smith, Heat recirculating reactors: Fundamental research and applications, Prog. Energ. Combust. 72 (2019) 32–58.

[5] F. J. Weinberg, Combustion Temperatures: The Future?, Nature 233 (1971) 239–241.

[6] G. De Soete, Stability and propagation of combustion waves in inert porous media, Symp. (Int.) Combust. 11 (1967) 959–966.

[7] T. Takeno, K. Sato, An excess enthalpy flame theory, Combust. Sci. Technol. 20 (1979) 73–84.

[8] T. Takeno, K. Sato, K. Hase, A theoretical study on an excess enthalpy flame, Symp. (Int.) Combust. 18 (1981) 465–472.

[9] B. Deshaies, G. Joulin, Asymptotic study of an excess-enthalpy flame, Combust. Sci. Technol. 22 (1980) 281–285.

[10] F. M. Pereira, A. A. Oliveira, F. F. Fachini, Asymptotic analysis of stationary adiabatic premixed flames in porous inert media, Combust. Flame 156 (2009) 152–165.

[11] F. Pereira, A. Oliveira, F. Fachini, Theoretical analysis of ultra-lean premixed flames in porous inert media, J. Fluid Mech. 657 (2010) 285–307.

[12] F. M. Pereira, A. A. Oliveira, F. F. Fachini, Maximum superadiabatic temperature for stabilized flames within porous inert media, Combust. Flame 158 (2011) 2283–2288.

[13] P.-A. Masset, O. Dounia, L. Selle, Fully explicit formulae for flame speed in infinite and finite porous media, Combust. Theor. Model. (2021) 1–28.

[14] P.-A. Masset, O. Dounia, L. Selle, Fully explicit formulae for flame speed in infinite and finite porous media, Combust. Theory Model. 25 (2021) 1–28.

[15] M. Sahraoui, M. Kaviany, Direct simulation vs volume-averaged treatment of adiabatic, premixed flame in a porous medium, Int. J. Heat Mass Tran. 37 (1994) 2817–2834.

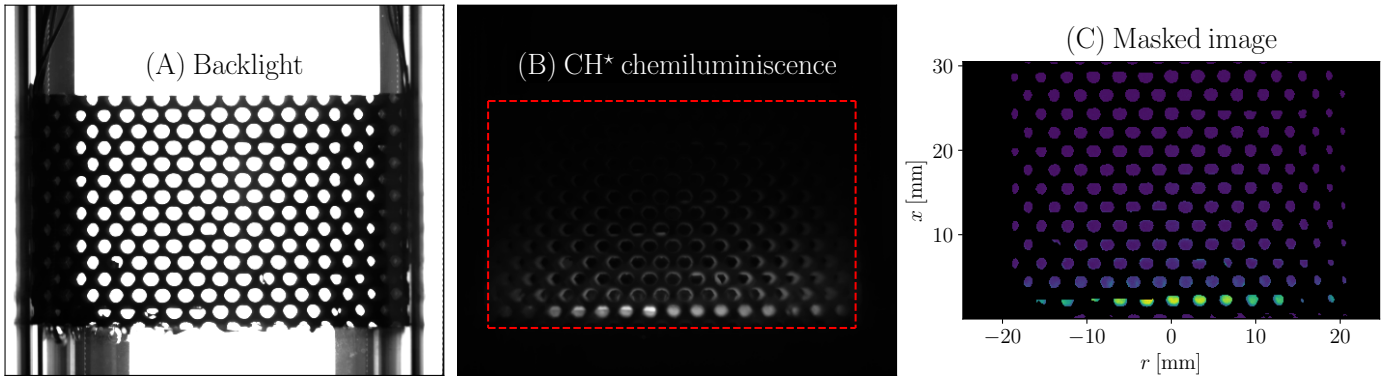

Figure A.9: (A) Backlight image. (B) CH⋆ chemiluminiscence signal. (C) Masked and cropped image

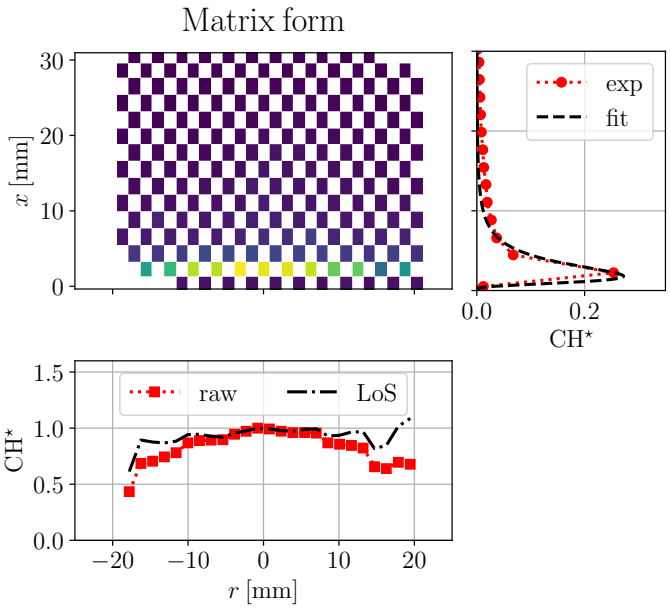

Figure A.10: Matrix form of the CH⋆ chemiluminiscence image from which the axial and radial profiles of CH⋆ are computed.

[16] C. Hackert, J. Ellzey, O. Ezekoye, Combustion and heat transfer in model two-dimensional porous burners, Combust. Flame 116 (1999) 177–191.

[17] C. Bedoya, I. Dinkov, P. Habisreuther, N. Zarzalis, H. Bockhorn, P. Parthasarathy, Experimental study, 1d volume-averaged calculations and 3d direct pore level simulations of the flame stabilization in porous inert media at elevated pressure, Combust. Flame 162 (2015) 3740–3754.

[18] J. C. Ferguson, S. Sobhani, M. Ihme, Pore-resolved simulations of porous media combustion with conjugate heat transfer, Proc. Combust. Inst. 38 (2021) 2127–2134.

[19] P.-A. Masset, F. Duchaine, A. Pestre, L. Selle, Modelling challenges of volume-averaged combustion in inert porous media, Combust. Flame 251 (2023) 112678.

[20] F. Muller, O. Dounia, L. Selle, Direct pore-level simulation of hydrogen flame anchoring mechanisms in an inert porous media, Phys. Fluids 36 (2024).

[21] E. Boigné, T. Zirwes, D. Y. Parkinson, G. Vignat, P. Muhunthan, H. S. Barnard, A. A. MacDowell, M. Ihme, Integrated experimental and computational analysis of porous media combustion by combining gas-phase synchrotron μct, ir-imaging, and pore-resolved simulations, Combust. Flame 259 (2024) 113132.

[22] J. Howell, M. Hall, J. Ellzey, Combustion of hydrocarbon fuels within porous inert media, Prog. Energy Combust. Sci. 22 (1996) 121–145.

[23] J. Dunnmon, S. Sobhani, M. Wu, R. Fahrig, M. Ihme, An investigation of internal flame structure in porous media combustion via X-ray Computed Tomography, Proc. Combust. Inst. 36 (2017) 4399–4408.

[24] I. Malico, J. C. Pereira, Numerical predictions of porous burners with integrated heat exchanger for household applications, J. Porous Media 2 (1999).

[25] T. Zirwes, G. Vignat, E. R. Toro, E. Boigné, K. Younes, D. Trimis, M. Ihme, Improving volume-averaged simulations of matrix-stabilized combustion through direct x-ray μct characterization: Application to nh3/h2-air combustion, Combust. Flame 257 (2023) 113020.

[26] G. Vignat, T. Zirwes, E. R. Toro, K. Younes, E. Boigné, P. Muhunthan, L. Simitz, D. Trimis, M. Ihme, Experimental and numerical investigation of flame stabilization and pollutant formation in matrix stabilized ammonia-hydrogen combustion, Combust. Flame 250 (2023) 112642.

[27] P.-A. Masset, Modelling challenges of stationary combustion in inert porous media, Ph.D. thesis (2022).

[28] N. Djordjevic, P. Habisreuther, N. Zarzalis, A numerical investigation of the flame stability in porous burners employing various ceramic sponge-like structures, Chem. Eng. Sci. 66 (2011) 682–688.

[29] F. Kuwahara, M. Shirota, A. Nakayama, A numerical study of interfacial convective heat transfer coefficient in two-energy equation model for convection in porous media, Int. J. Heat Mass Transfer 44 (2001) 1153–1159.

[30] M. B. Saito, M. J. De Lemos, A correlation for interfacial heat transfer coefficient for turbulent flow over an array of square rods, J. Heat Transfer 128 (2006) 444–452.

[31] B. Stelzner, C. Keramiotis, S. Voss, M. Founti, D. Trimis, Analysis of the flame structure for lean methane–air combustion in porous inert media by resolving the hydroxyl radical, Proc. Combust. Inst. 35 (2015) 3381–3388.

[32] J. Kiefer, M. Weikl, T. Seeger, F. Von Issendorff, F. Beyrau, A. Leipertz, Non-intrusive gas-phase temperature measurements inside a porous burner using dual-pump CARS, Proc. Combust. Inst. 32 (2009) 3123–3129.

[33] M. Weikl, S. Tedder, T. Seeger, A. Leipertz, Investigation of porous media combustion by coherent anti-stokes raman spectroscopy, Exp. Fluids 49 (2010) 775–781.

[34] R. V. Fursenko, I. A. Yakovlev, E. S. Odintsov, S. D. Zambalov, S. S. Minaev, Pore-scale flame dynamics in a one-layer porous burner, Combust. Flame 235 (2022) 111711.

[35] S. Sobhani, P. Muhunthan, E. Boigné, D. Mohaddes, M. Ihme, Experimental feasibility of tailored porous media burners enabled via additive manufacturing, Proc. Combust. Inst. 38 (2021) 6713–6722.

[36] A. C. Contini, F. M. Pereira, Numerical study of flame stability within inert porous media with variable void area, Combust. Flame 246 (2022) 112475.

[37] S. Sobhani, D. Mohaddes, E. Boigne, P. Muhunthan, M. Ihme, Modulation of heat transfer for extended flame stabilization in porous media burners via topology gradation, Proc. Combust. Inst. 37 (2019) 5697–5704.
[38] S. Sobhani, S. Allan, P. Muhunthan, E. Boigne, M. Ihme, Additive manufacturing of tailored macroporous ceramic structures for high-temperature applications, Adv. Eng. Mater. 22 (2020) 2000158.
[39] C. Y. Yap, C. K. Chua, Z. L. Dong, Z. H. Liu, D. Q. Zhang, L. E. Loh, S. L. Sing, Review of selective laser melting: Materials and applications, Appl. Phys. Rev. 2 (2015) 041101.
[40] H. Karcher, K. Polthier, Construction of triply periodic minimal surfaces, Philos. Trans. R. Soc. London, Ser. A 354 (1996) 2077–2104.
[41] I. Maskery, L. Sturm, A. O. Aremu, A. Panesar, C. B. Williams, C. J. Tuck, R. D. Wildman, I. A. Ashcroft, R. J. Hague, Insights into the mechanical properties of several triply periodic minimal surface lattice structures made by polymer additive manufacturing, Polymer 152 (2018) 62–71.
[42] W. H. Meeks III, The theory of triply periodic minimal surfaces, Indiana Univ. Math. J. (1990) 877–936.
[43] D. G. Goodwin, R. L. Speth, H. K. Moffat, B. W. Weber, Cantera: An object-oriented software toolkit for chemical kinetics, thermodynamics, and transport processes, 2018. doi:10.5281/zenodo.1174508, version 2.4.0.
[44] G. P. Smith, Gri-mech 3.0, http://www. me. berkley. edu/gri_mech/ (1999).
[45] A. J. Barra, J. L. Ellzey, Heat recirculation and heat transfer in porous burners, Combust. Flame 137 (2004) 230–241.
[46] F. E. Teruel, Entrance effect on the interfacial heat transfer and the thermal dispersion in laminar flows through porous media, Int. J. Therm. Sci. 104 (2016) 172–185.
[47] N. Wakao, S. Kagei, Heat and mass transfer in packed beds, volume 1, Taylor & Francis, 1982.
[48] A. Zukauskas, Heat transfer from tubes in crossflow, in: Advances in heat transfer, volume 8, Elsevier, 1972, pp. 93–160.
[49] J. T. Gostick, Z. A. Khan, T. G. Tranter, M. D. Kok, M. Agnaou, M. Sadeghi, R. Jervis, Porespy: A python toolkit for quantitative analysis of porous media images, J. Open Source Softw. 4 (2019) 1296.
[50] J. Gostick, M. Aghighi, J. Hinebaugh, T. Tranter, M. A. Hoeh, H. Day, B. Spellacy, M. H. Sharqawy, A. Bazylak, A. Burns, W. Lehnert, A. Putz, Openpnm: A pore network modeling package, Comput. Sci. Eng. 18 (2016) 60–74.
[51] J. C. Simmons, X. Chen, A. Azizi, M. A. Daeumer, P. Y. Zavalij, G. Zhou, S. N. Schiffres, Influence of processing and microstructure on the local and bulk thermal conductivity of selective laser melted 316l stainless steel, Addit. Manuf. 32 (2020) 100996.
[52] M. Balat-Pichelin, J. Sans, E. Bêche, Spectral directional and total hemispherical emissivity of virgin and oxidized 316l stainless steel from 1000 to 1650 k, Infrared Phys Technol 123 (2022) 104156.
[53] P.-A. Masset, O. Dounia, L. Selle, Combustion regimes in inert porous media: From decoupled to hyperdiffusive flames, Combust. Flame 241 (2022) 112052.